Stewart, AW.; Bouich, A.; Marí, B. (2021). Inorganic perovskites improved film and crystal quality of CsPbIBr2 when doped with rubidium. Journal of Materials Science Materials in Electronics. 32(20):24825-24833. https://doi.org/10.1007/s10854-021-06941-z

Stewart AW, Bouich A, Marí B (2021) Inorganic perovskites improved film and crystal quality of CsPbIBr2 when doped with rubidium. J Mater Sci Mater Electron 1–9. https://doi.org/10.1007/s10854-021-06941-z

Inorganic-Perovskites: Improved Film and Crystal Quality of $CsPbIBr_2$ when Doped with Rubidium

Alexander W. Stewart[a], Amal Bouich[a,b,*], Bernabé Marí[a]

[a] Institut de Disseny i Fabricació, Universitat Politècnica de València

Camí de Vera, València, Spain 46022

[b] Laboratory (LMEE), University of Ibn Tofail

Av. de L'Université, Kenitra, Morocco BP 242

*Corresponding autor email: **Bouich.amal@gmail.com**

Abstract:

In this work $CsPbIBr_2$ is doped with rubidium, where up to 12% of caesium atoms are replaced with those of rubidium. The obtained $Cs_{1-x}Rb_xPbIBr_2$, x= (0, 0.02, 0.04, 0.06, 0.08, 0.10, 0.12), films were characterized by X-ray diffraction (XRD), the scanning electron microscope (SEM), photo-luminescence (PL) and UV-visible spectroscopy. The integration of Rb^+ ions into the lattice leads to a detectable change in opto-electronic and morphological structure. Substituting 6% of caesium atoms yields the best results, eliminating pinholes, and elevating crystallite size and absorption coefficient by 116% and 125%, respectively. Other novel observations, of particular interest, include a slight increase in band-gap energy from 2.1eV to 2.14eV, and a decrease in stability. Over a period of 15 days, where temperature and relative humidity kept at 23°C and 20% respectively, a larger amount of degradation was seen to take place as rubidium content was increased. Therefore, the doping of $CsPbIBr_2$ with rubidium is most useful in the case where specifically film and crystal quality are desired to be targeted.

Keywords: $CsPbIBr_2$, Inorganic-Perovskites, Thin Films, Morphology

Graphical Abstract:

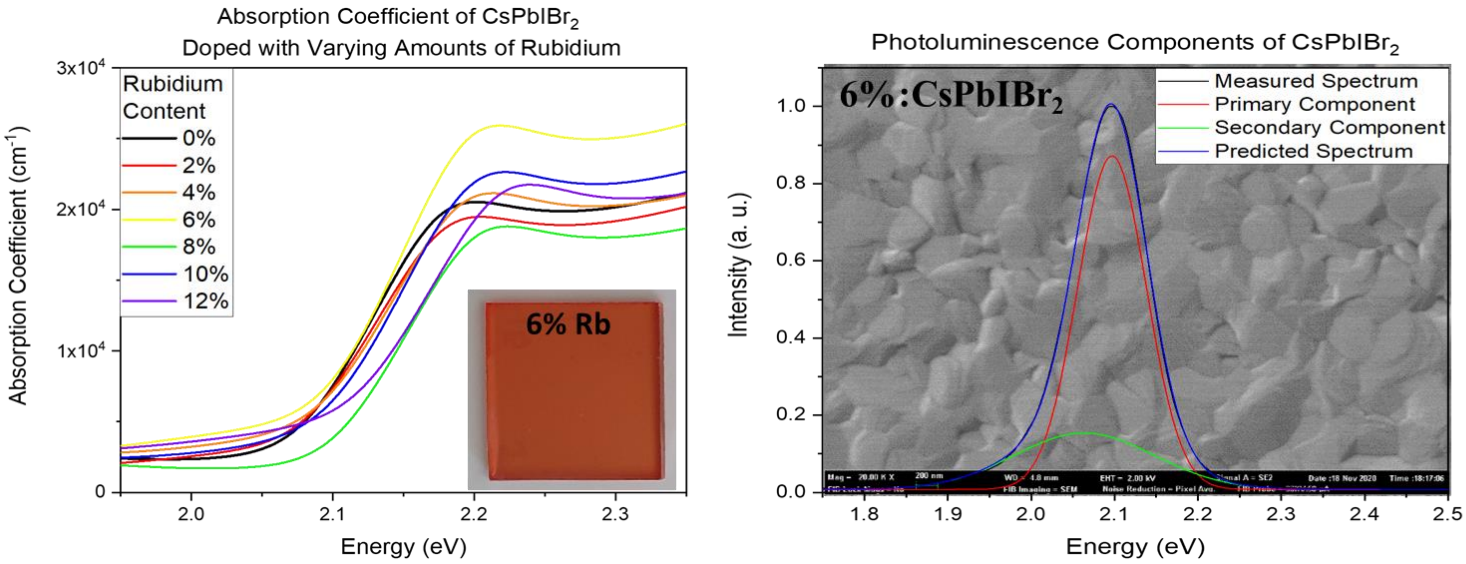

Highlight:

The incorporation of Rb^+ ions into the lattice leads to a detectable change in opto-electronic and morphological structure.

Substituting 6% of caesium atoms yields the best results, eliminating pinholes, and elevating crystallite size and absorption coefficient by 116% and 125%, respectively.

The incorporation of Rb^+ ions lead a slight increase in band-gap energy from 2.1eV to 2.14eV, and a decrease in stability.

1 Introduction

The rise of perovskite solar cells (PSCs) has been accompanied by an unprecedented increase in power conversion efficiency (PCE), from 3.8% to 25.5%, in just over a decade [1,2]. Perovskites are crystal structures of the composition ABX_3. In many cases, they can be predicted using the Goldschmidt tolerance and the octahedral-factor [3–5]. Furthermore, they tend to have a cubic, tetragonal, or orthorhombic structure corresponding to a high, intermediate, low temperature phase, respectively [6]. Methylammonium-based devices catapulted perovskites into the spotlight, having shown exceptional optoelectronic properties including high absorption coefficients, long-carrier lifetimes, favourable spin-orbit coupling, low exciton binding-energy, high proportions of free carriers, high mobilities and large diffusion lengths [7–11]. The combination of these outstanding properties with perovskite's low-cost and high scalability, demonstrates why these materials have gained such notoriety in the photovoltaic community [12]. That said, there remains one fundamental property which plagues methylammonium-devices, and that is their inherent instability. This is catalysed by moisture, radiation and temperature, factors which the PSC will unavoidably be exposed to during its working life [13–16].

Since methylammonium-based devices degrade irreversibly back into the precursor components, one of which is volatile, partial substitution with an inorganic cation such as caesium arose as a way to harness the aforementioned opto-electronic properties while increasing stability [16,17]. Similarly, this idea was taken further, and completely inorganic devices were investigated. While $CsPbI_3$-based devices showed desirable band-gaps, they too demonstrated degradation, albeit via a reversible phase change [18]. On the other hand, $CsPbBr_3$ showed exceptional stability, however this came at the cost of increasing the band-

gap. For these reasons, iodine-bromine alloys such as $CsPbI_2Br$ and $CsPbIBr_2$ became of interest. These alloys strike a compromise between band-gap and stability, the latter being the subject of this work [19,20].

To date, the highest obtained PCE for a $CsPbIBr_2$ based device is 10.71%, which is just over half of the Shockley-Queisser limit, thus revealing research opportunities in the field [21,22]. For tables on device PCEs and an overview of the field, see [22,23]. While the relatively high band-gap of $CsPbIBr_2$ will limit its use in single-junction cells, its true potential may be harnessed as a top-cell in a multi-junction, as highlighted by Oxford-PV's recent breakthrough [24,25]. Until now, devices have been prepared via one-step spin-coating, a gas-assisted method, spray-assisted deposition, dual-source thermal evaporation and two-step spin-coating [20,22,26–30]. As it stands, one of the biggest problems in the field is the consistent deposition of high-quality films, with many reporting a high number of pinholes and small grain sizes [20,23,26,29]. Some of the methods investigated to improve films include: the use of antisolvent to improve coverage and morphology, guanidinium iodide for surface passivation, adding a small amount of $PbCl_2$ to the precursor solution, light soaking, intermolecular exchange, precursor solution aging, band alignment via interface engineering and doping with Magnesium [22,23,26,30]. The latter being related most closely to this work, where the effects of doping $CsPbIBr_2$ with rubidium is investigated. While doping with Rb^+ ions has been shown to have a beneficial effect on the sister materials $CsPbIBr_2$ and $CsPbBr_3$, as of yet, there appears to be a lack of equivalent research carried out on $CsPbIBr_2$[31–33].

2 Methodology

Materials: All chemicals were purchased from Tokyo Chemical Industry unless otherwise stated in parenthesis. The precursor solution consisted of caesium iodide (CsI), lead bromide ($PbBr_2$) and rubidium iodide (RbI, 99% from Alfa Aesar), dissolved in dimethyl sulfoxide (DMSO 99.9%).

Thin film preparation: The $Cs_{1-x}Rb_xPbIBr_2$ thin films were deposited on top of fluorine-doped tin oxide (FTO) substrates (TEC 15A) by one step spin coating technique, with an area of $2.5cm^2$, purchased from XOP Glass. Substrates were cleaned for 15 minutes in detergent, ethanol (LabKem), acetone (VWR Chemicals) and isopropanol (VWR Chemicals) in an ultrasonic bath before a further 15 minutes in the UV-Ozone, manufactured by Ossila. The $CsPbIBr_2$ precursor solution was prepared by allowing CsI and $PbBr_2$ to dissolve completely in DMSO (1 mL), at room temperature. To dope $CsPbIBr_2$ with RbI, 0.5M solutions with molar ratios of $100 - x: x:\ 100$ (CsI: RbI: $PbBr_2$) were prepared, where x is the rubidium doping percentage. after the solution was mixed at 85 temperature and Solutions were left to heat overnight in the glovebox. Samples were statically spin coated at 3500 RPM for 30 seconds, after which they were annealed for 5 minutes at 50˚C and then 250˚C. Samples were stored in inert N_2 atmosphere until used.

Characterization techniques: Thin films of $Cs_{1-x}Rb_xPbIBr_2$, where x = 0%, 2%, 4%, 6%, 8%, 10% and 12%, were characterized by X-ray diffraction (XRD) using the RIGAKU Ultima IV with Cu kα radiation (λ = 1.5418 Å). Morphology images were taken using the scanning electron microscope (SEM) Quanta 200-FEI with an applied voltage of 1.5 kV. Optical properties were performed with an Ocean Optics HR4000 spectrophotometer and photoluminescence (PL) emission was driven by an He-Cd laser with a wavelength of λ = 405 nm.

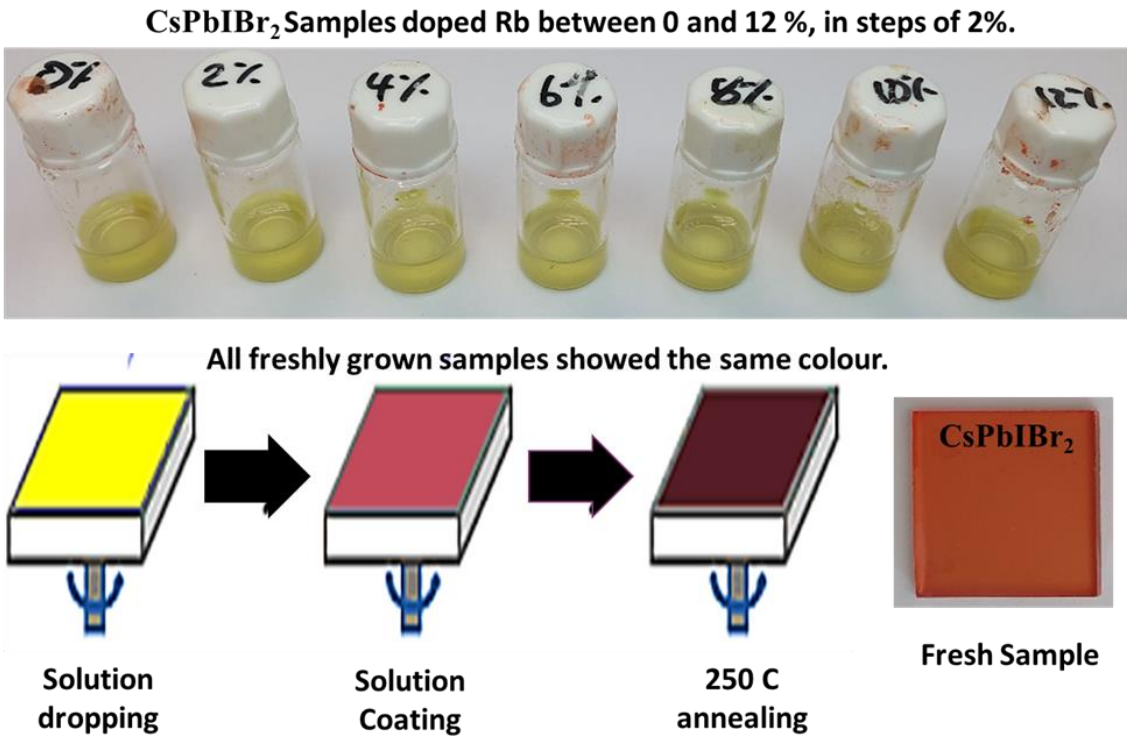

Figure 1: Schematic of the one-step spin-coating procedure for the mixed-halide perovskite $Cs_{1-x}Rb_xPbIBr_2$, where x = 0%, 2%, 4%, 6%, 8%, 10% and 12%.

3 Results and Discussion

To characterize the X-ray diffraction (XRD) peaks, a Rietveld Refinement was carried out. The refinement itself was found to be exceptionally precise, with R_{wp} = 5.94% and R_p = 4.30% (Figure 2 (b)). These values reflect the accordance between the predicted and measured spectra, with 0% corresponding to identical curves. The crystals were found to be strongly oriented in the (100) plane, with the bright peaks at 14.9° and 30.1°corresponding to the (100) and (200) indices. A small peak at 22° is believed to be attributed to the (110) plane. These results are in accordance with the literature [22,26,33], except for one study that found an orthorhombic structure with the primary peak at 30° belonging to the (220) plane [29]. The lattice was found to be tetragonal, and belonging to the Pm-3m space group, with a=b=5.93278 ±0.00030 and c=5.88519 ± 0.00842. These results are in accordance with those found elsewhere [23,34].(see Fig.1 in supplementary materials)

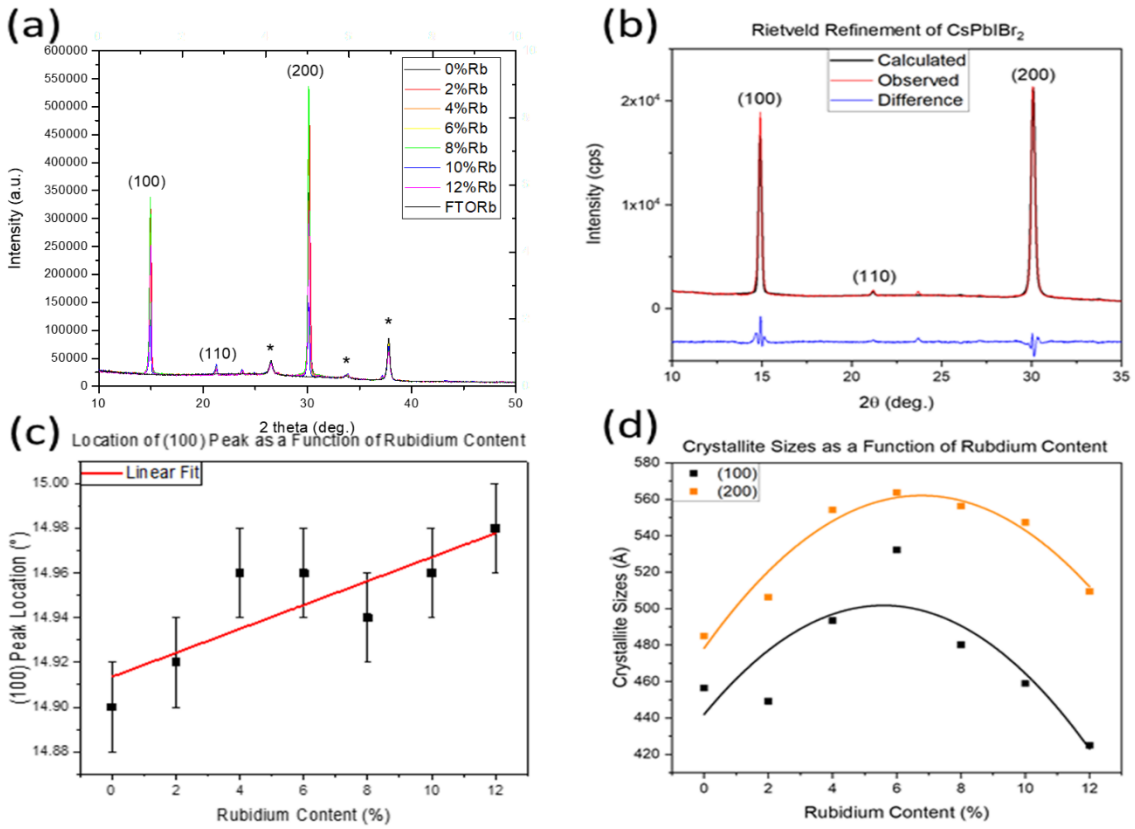

Figure 2: XRD results (a) XRD pattern perovskite $Cs_{1-x}Rb_xPbIBr_2$, where x = 0%, 2%, 4%, 6%, 8%, 10% and 12%. (b) Rietveld Refinement of reference sample ($CsPbIBr_2$ with no doping) (c) The location of the (100) peak as rubidium content is increased. The error bars correspond to the resolution of the equipment. Similar results are obtained for the (200) peak. (d) Crystallite sizes calculated from the FWHM of the major diffraction peaks corresponding to the (100) and (200) planes

Table 1. The grain size, the full width at half maximum (FWHM) , dislocation density and lattice strain of XRD of $Cs_{1-x}Rb_xPbIBr_2$, where x = 0%, 6%, 8% and 12%thin films

Sample.ID	Grain size (nm)	FWHM (deg)	Dislocation density (cm^{-1})	Lattice strain (e)
Pure	480	0.1833	0.50×10^{-5}	0.40
6% Rb	570	0.1572	0.39×10^{-5}	0.65
12 % Rb	420	0.1969	0.59×10^{-5}	0.28

Interestingly, it seems that the full width at half maximum (FWHM) of the main diffraction peaks reaches its narrowest when 6% of caesium atoms are substituted with rubidium (see Fig.2 in supplementary materials). Application of the Scherrer equation reveals that crystallite sizes take an approximately parabolic form, with a maximum at 6% [35]. This maximum corresponds to an increase in crystallite size of 117% and 116%, corresponding to the (100) and (200) peaks respectively, when compared to the non-doped sample. As the concentration of rubidium ions in the precursor solution was increased, all the peaks in the sample were systematically shifted. This can be seen for the (200) and (100) plane (Figure 2 (d)). This is likely attributable to the fact that Rb+ (1.52A) has a smaller ionic radius than Cs+ (1.67A), therefore a shift to higher angles correspond to a contraction of the unit cell [33]. Moreover, the contraction of the unit cell suggests that rubidium ions are substituting caesium rather than occupying interstitial sites.

To independently confirm the insertion of rubidium into the lattice, energy-dispersive X-ray spectroscopy (EDS) was performed (see Fig 2 in supplementary materials). Given that Rb^+ ions substitute Cs^+ ions as A site cations, it is possible to determine their population as

$$Rb^+_{population} = \frac{Rb^+\%}{Rb^+\% + Cs^+\%} \times 100 \qquad (1)$$

Where $Rb^+\%$ and $Cs^+\%$ are the atomic percentages measured. Plotting this against precursor concentration yields a linear relationship with $Rb^+_{population} \approx Rb^+_{precursor}$, suggesting that all the rubidium precursor is fully integrated into the structure (Figure 3(b)).

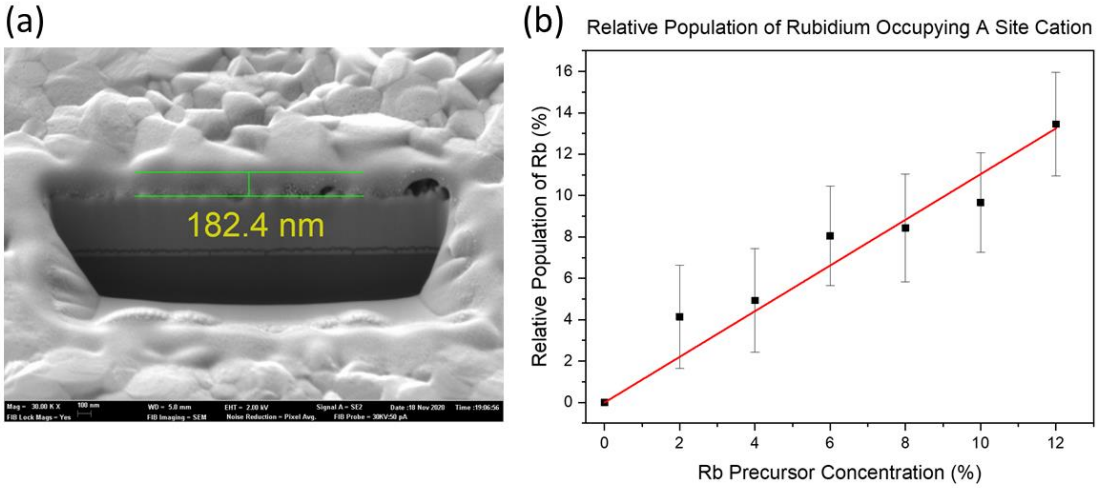

Figure 3: (a) SEM image taken during the measurement of the 6% sample's thickness (b) Measured dopant percentage as a function of dopant precursor percentage. Error bars show one standard deviation in the measurement.

Using the focused ion beam (FIB) it was possible to design a cut in the sample, allowing the thickness of the sample to be measured (Figure 3 (a)). Carrying out this process for all samples, an average thickness of 195nm was found, with a standard deviation of 13nm.

Observations carried out using the scanning electron microscope (SEM) revealed that the sample doped with 6% rubidium had the best quality overall, with no pinholes and uniform coverage (see Figure 4). The reference sample showed an abundance of pinholes, however increasing the rubidium content caused a decrease in the density of pinholes. Once the rubidium concentration was increased past 6%, the film quality decreased. This can be seen in the 8% sample (Figure 4 (d)) where small pinholes are beginning to form once more. It is believed that these pinholes form when pockets of solvent remain within the material during the crystallization process [23]. Measuring the absorbance of the freshly prepared samples, it was possible to calculate their absorption spectrum using the thickness values (Figure 5 (a)). All samples have an absorption coefficient of around 2×10^4 cm^{-1} above 2.2eV and show the onset of the optical band edge around 2.07eV (≈600nm), which agrees with values found elsewhere [20,29]. Whilst most samples had a comparable absorption coefficient to the non-doped sample, the 6% sample increased by 125%. Intuitively, this makes sense, since the 6% sample showed no pinholes in SEM (Figure 4 (c)) and larger crystallite sizes (Figure 2(d)), suggesting it would be a more effective absorber. It should be noted, however, that the absorption coefficient scales inversely with layer thickness and as such the precision of these values are limited by the methods employed previously (Figure 3(a)) [20,29]. Employing the Tauc plot to estimate the band-gap, band-gap values increased slightly, from 2.1 to 2.14eV, as rubidium content was increased. Similar parts of the spectra were taken for the linear fit, to minimize any random errors (Figure 5(b)).

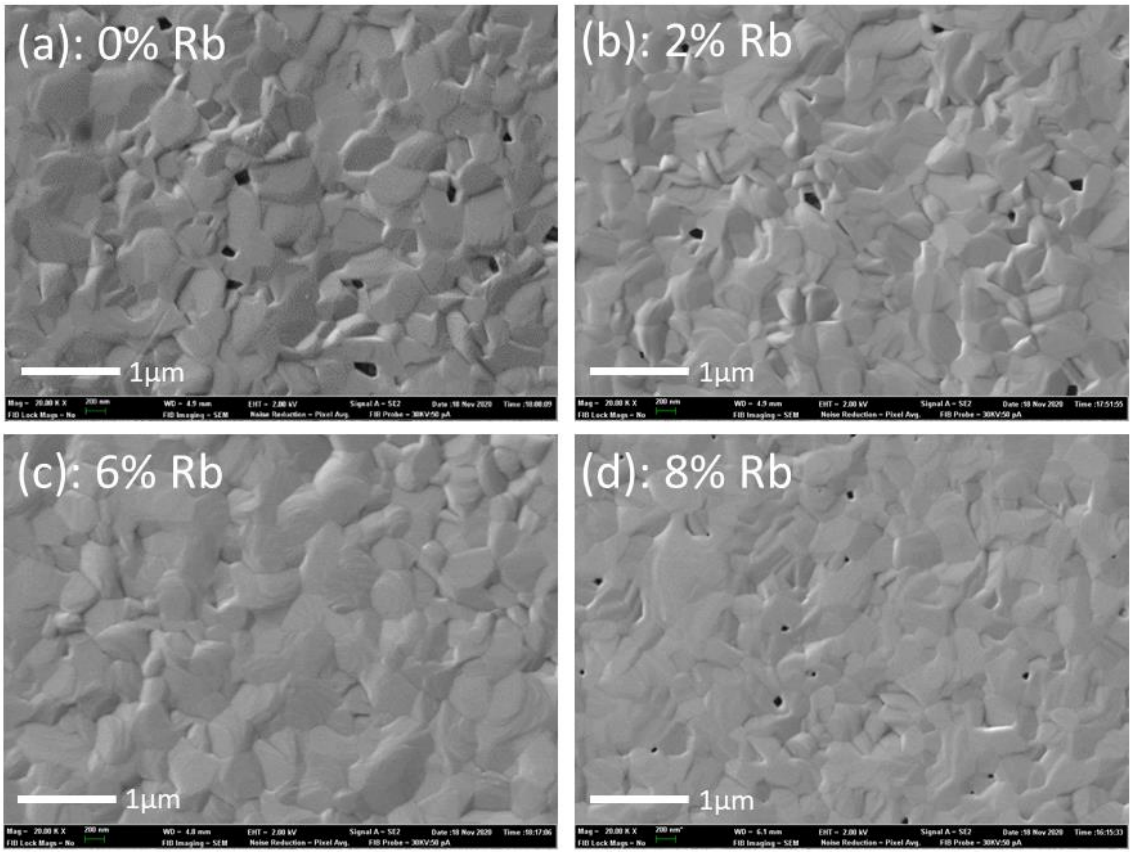

Figure 4: SEM images, at 20,000 times magnification, of $CsPbIBr_2$ doped with (a) no rubidium (reference sample), where large pinholes can be seen (b) 2% rubidium, where pinhole size and density are seen to decrease with respect to the reference sample (c) 6% rubidium, no pinholes (d) 8% rubidium, were small pinholes are formed.

To model the photo-luminescence (PL) spectra taken, a predicted spectrum was constructed by summing two Gaussian functions of the form

$$y = y_0 + \frac{A}{\omega\sqrt{\pi/2}} e^{-\frac{2(x-x_c)^2}{\omega^2}} \qquad (2)$$

Where y_0, A, x_c and ω are constants. Using this method, it was possible to discern a primary and secondary component of a given PL spectrum (Figure 5(c)). The R^2 value is a statistical measure of the similarity between curves, in the case that they are identical it is equal to 1. For these models, all R^2 values lay above 0.996, except for the 4% sample which had significantly more background noise. It is thought that the secondary components of the PL spectra arise, under illumination, due to the formation of iodine rich phases [28] (see Table 1 in supplementary materials).

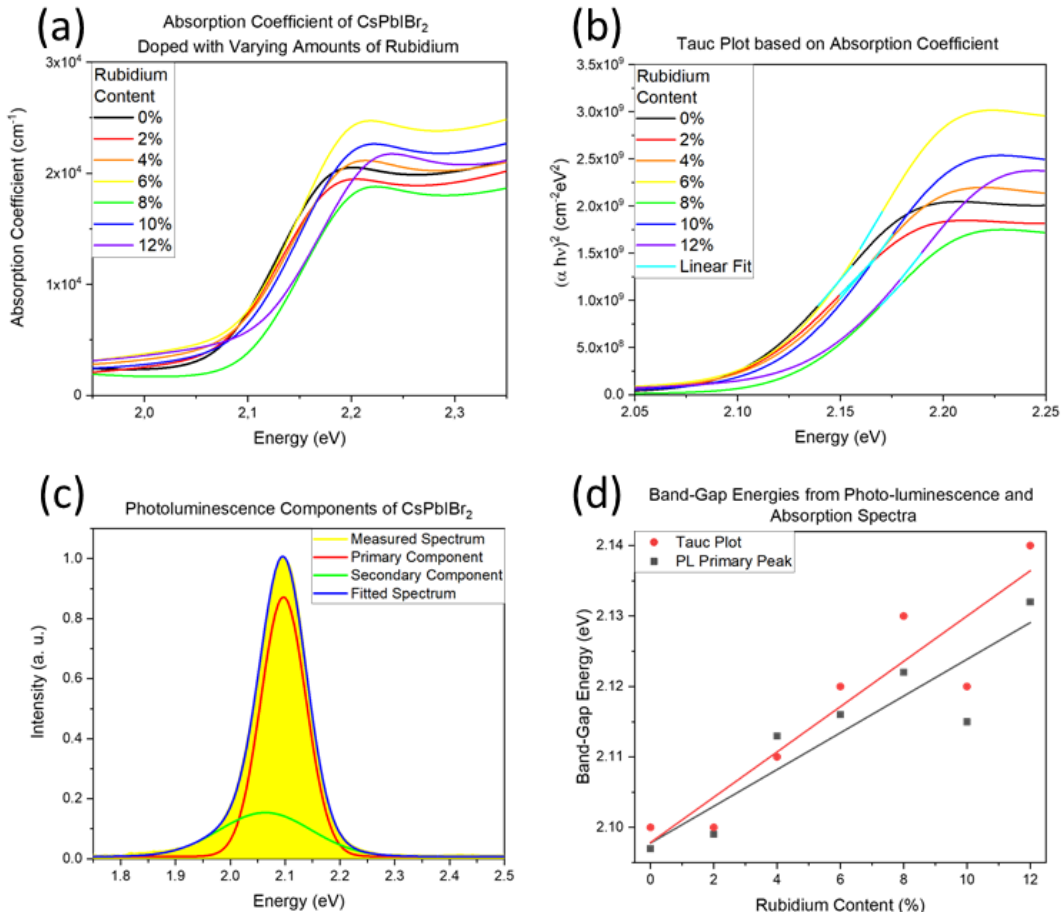

Figure 5: (a) Absorption coefficients of the freshly prepared samples (b) Bandgap estimation using the Tauc plot (c) Decomposition of the reference sample´s PL spectrum into components (d) band-gap values calculated from PL and the Tauc plot.

Combining the results from PL measurements with those from the absorption coefficient, it can be said that an increase in band-gap is almost certainly taking place as elevated quantities of rubidium are incorporated into the lattice (Figure 5 (d)). Given the limitations of the Tauc plot, band-gap values are almost perfectly in accordance with those taken from the primary PL component. Moreover, both techniques yield the desired band-gap value for the reference sample [20,23,26,29]. To investigate the effect of rubidium incorporation on the stability $CsPbIBr_2$, the absorption coefficients were measured after the samples had been stored in ambient conditions (Figure 6 (a)). A batch of newly synthesized samples were kept in the laboratory for 15 days, during which temperature and relative humidity kept constant, at 23°C and 20% respectively.

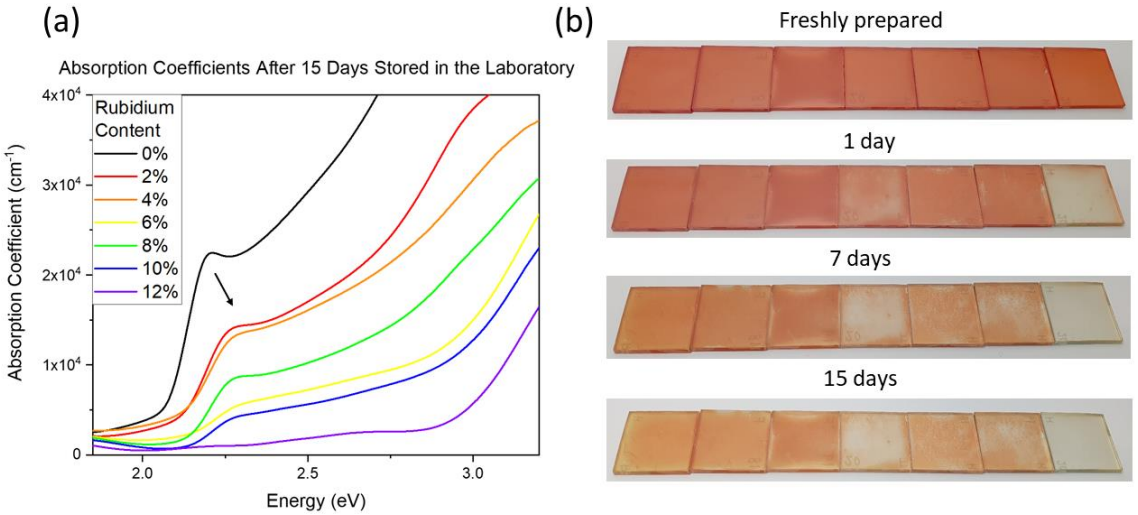

Figure 6: (a) Absorption coefficients of $CsPbIBr_2$ doped with varying amounts of rubidium (b) Photos where degradation can be seen to be taking place in the samples over the study.

In general, higher rubidium content is shown to correlate with accelerated degradation, demonstrated by films with larger quantities of Rb experiencing larger shifts in energy (Figure 6 (a)). Most likely, the absorption coefficient curves shifting to higher energies corresponds to a progressive change from the meta-stable high-temperature α-phase towards the intermediate-temperature δ-phase, which is stable at room temperature. The shift is especially pronounced for the 12% sample, which had changed phase within one day (Figure 6 (b)). It is possible that due to the decreased ionic radius of rubidium, the volumetric ratio between the PbX_6 octahedra and A-site cations decreases, aggravating its thermodynamic instability [18].

4 Conclusion

In this study, the effect of rubidium incorporation in the $CsPbIBr_2$ lattice is investigated via XRD, SEM, EDS and optical measurements. The correct incorporation of rubidium is independently confirmed from XRD peak shifts and EDS results. Grain size is shown to be a function of dopant content, taking its maximum value when 6% of caesium atoms are replaced with rubidium. SEM measurements reveal that the methodology yields layers with an average thickness of 195nm (σ = 13nm). In terms of morphology, the incorporation of rubidium, up to 6%, seems to favourably affect film coverage by decreasing pinholes. Optical measurements reveal that samples have an absorption coefficient around 2×10^4 cm^{-1} above 2.2eV, with the 6% sample having a superior absorption coefficient. Absorption coefficient and PL measurements both suggest a slight increase in band-gap as rubidium content is increased. Overall, the sample with 6% rubidium showed the best results. Investigation into the stability of the prepared samples reveals that rubidium incorporation has an adverse effect on stability. While doping $CsPbIBr_2$ with rubidium seems to decrease stability, the technique brings a myriad of improvements to the crystal and film quality. As such it should be considered as a useful tool when developing high quality thin films.

Acknowledgements

This work was supported by Ministerio de Economía y Competitividad (Grant Number PID2019-107137RB-C21). One of the authors A.W.S. acknowledges the Generalitat Valenciana and the EU for financial support (ACIF/2020/286).

Declaration of Interest

- All authors have participated in (a) conception and design, or analysis and interpretation of the data; (b) drafting the article or revising it critically for important intellectual content; and (c) approval of the final version.

- This manuscript has not been submitted to, nor is under review at, another journal or other publishing venue.

- The authors have no affiliation with any organization with a direct or indirect financial interest in the subject matter discussed in the manuscript

- The following authors have affiliations with organizations with direct or indirect financial interest in the subject matter discussed in the manuscript:

Author's name	Affiliation
Alexander Wyn Stewart	Polytechnic University of Valencia
Amal Bouich	Polytechnic University of Valencia
Bernabé Marí Soucase	Polytechnic University of Valencia

Bibliography

1. Kojima, A., Teshima, K., Shirai, Y. & Miyasaka, T. Organometal halide perovskites as visible-light sensitizers for photovoltaic cells. *J. Am. Chem. Soc.* **131**, 6050–6051 (2009).
2. Best Research-Cell Efficiency Chart | Photovoltaic Research | NREL. https://www.nrel.gov/pv/cell-efficiency.html.
3. Goldschmidt, V. M. Die Gesetze der Krystallochemie. *Naturwissenschaften* **14**, 477–485 (1926).
4. Bartel, C. J. *et al.* New tolerance factor to predict the stability of perovskite oxides and halides. *Sci. Adv.* **5**, eaav0693 (2019).
5. Bouich, A., Ullah, S., Marí, B., Atourki, L., & Touhami, M. E. (2021). One-step synthesis of FA1-xGAxPbI3 perovskites thin film with enhanced stability of alpha (α) phase. Materials Chemistry and Physics, 258, 123973.
6. Miyata, A. *et al.* Direct measurement of the exciton binding energy and effective masses for charge carriers in organic-inorganic tri-halide perovskites. *Nat. Phys.* **11**, 582–587 (2015).
7. Wang, T. *et al.* Indirect to direct bandgap transition in methylammonium lead halide perovskite. *Energy Environ. Sci.* **10**, 509–515 (2017).
8. D'Innocenzo, V. *et al.* Excitons versus free charges in organo-lead tri-halide perovskites. *Nat. Commun.* **5**, (2014).
9. Herz, L. M. Charge-Carrier Mobilities in Metal Halide Perovskites: Fundamental Mechanisms and Limits. *ACS Energy Letters* vol. 2 1539–1548 (2017).
10. Alcocer, M. J. P., Leijtens, T., Herz, L. M., Petrozza, A. & Snaith, H. J. Electron-Hole Diffusion Lengths Exceeding Trihalide Perovskite Absorber. *Science (80-.).* **342**, 341–344 (2013).
11. Bouich, A., Mari, B., Atourki, L., Ullah, S., & Touhami, M. E. (2021). Shedding Light on the Effect of Diethyl Ether Antisolvent on the Growth of (CH 3 NH 3) PbI 3 Thin Films. JOM, 73(2), 551-557.
12. Snaith, H. J. Perovskites: The emergence of a new era for low-cost, high-efficiency solar cells. *Journal of Physical Chemistry Letters* vol. 4 3623–3630 (2013).
13. Bidai, K., Ameri, M., Amel, S., Ameri, I., Al-Douri, Y., Varshney, D., & Voon, C. H. (2017). First-

principles calculations of pressure and temperature dependence of thermodynamic properties of anti-perovskite BiNBa3 compound. Chinese Journal of Physics, 55(5), 2144-2155.
14. Ilyas, A., Khan, S. A., Liaqat, K., & Usman, T. (2021). Investigation of the structural, electronic, magnetic, and optical properties of CsXO3 (X= Ge, Sn, Pb) perovskites: A first-principles calculations. Optik, 244, 167536.
15. Arar, R., Ouahrani, T., Varshney, D., Khenata, R., Murtaza, G., Rached, D., ... & Reshak, A. H. (2015). Structural, mechanical and electronic properties of sodium based fluoroperovskites NaXF3 (X= Mg, Zn) from first-principle calculations. Materials Science in Semiconductor Processing, 33, 127-135.
16. Feng, S., Guo, F., Zhang, Y., Miao, F., Wang, Z., Yuan, C., & Yang, K. (2021). Structural evolution, lattice dynamics, electronic and thermal properties of VH2 under high pressure. Solid State Communications, 330, 114287.
17. Saraf, R., Mathur, A., & Maheshwari, V. (2020). Polymer-controlled growth and wrapping of perovskite single crystals leading to better device stability and performance. ACS applied materials & interfaces, 12(22), 25011-25019..
18. Straus, D. B., Guo, S., Abeykoon, A. M. & Cava, R. J. Understanding the Instability of the Halide Perovskite CsPbI3 through Temperature-Dependent Structural Analysis. *Adv. Mater.* **32**, 1–8 (2020).
19. Mariotti, S. *et al.* Stability and Performance of CsPbI2Br Thin Films and Solar Cell Devices. *ACS Appl. Mater. Interfaces* **10**, 3750–3760 (2018).
20. Ma, Q., Huang, S., Wen, X., Green, M. A. & Ho-Baillie, A. W. Y. Hole Transport Layer Free Inorganic CsPbIBr2 Perovskite Solar Cell by Dual Source Thermal Evaporation. *Adv. Energy Mater.* **6**, 2–6 (2016).
21. Shockley, W. & Queisser, H. J. Detailed balance limit of efficiency of p-n junction solar cells. *J. Appl. Phys.* **32**, 510–519 (1961).
22. Zhu, W. *et al.* Band Alignment Engineering Towards High Efficiency Carbon-Based Inorganic Planar CsPbIBr2 Perovskite Solar Cells. *ChemSusChem* **12**, 2318–2325 (2019).
23. Guo, Y. *et al.* Inorganic CsPbIBr2-Based Perovskite Solar Cells: Fabrication Technique Modification and Efficiency Improvement. *Sol. RRL* **3**, 1–13 (2019).
24. Jošt, M., Kegelmann, L., Korte, L. & Albrecht, S. Monolithic Perovskite Tandem Solar Cells: A Review of the Present Status and Advanced Characterization Methods Toward 30% Efficiency. *Adv. Energy Mater.* **10**, (2020).
25. Oxford PV retakes tandem cell efficiency record – pv magazine International. https://www.pv-magazine.com/2020/12/21/oxford-pv-retakes-tandem-cell-efficiency-record/.
26. Zhang, B. *et al.* High-performance cspbibr2 perovskite solar cells: Effectively promoted crystal growth by antisolvent and organic ion strategies. *ACS Appl. Mater. Interfaces* **11**, 33868–33878 (2019).
27. Zhang, W. *et al.* Charge-Transporting-Layer-Free, All-Inorganic CsPbIBr 2 Perovskite Solar Cells Via Dipoles-Adjusted Interface. *Nanomaterials* (2020).
28. Li, W. *et al.* Phase Segregation Enhanced Ion Movement in Efficient Inorganic CsPbIBr2 Solar Cells. *Adv. Energy Mater.* **7**, 1–8 (2017).
29. Lau, C. F. J. *et al.* CsPbIBr2 Perovskite Solar Cell by Spray-Assisted Deposition. *ACS Energy Lett.* **1**, 573–577 (2016).
30. Liang, J. *et al.* Enhancing Optical, Electronic, Crystalline, and Morphological Properties of Cesium Lead Halide by Mn Substitution for High-Stability All-Inorganic Perovskite Solar Cells with Carbon Electrodes. *Adv. Energy Mater.* **8**, 1–7 (2018).
31. Patil, J. V., Mali, S. S. & Hong, C. K. A-Site Rubidium Cation-Incorporated CsPbI2Br All-Inorganic Perovskite Solar Cells Exceeding 17% Efficiency. *Sol. RRL* **4**, 1–9 (2020).
32. Guo, Y. *et al.* Efficient and Hole-Transporting-Layer-Free CsPbI 2 Br Planar Heterojunction Perovskite Solar Cells through Rubidium Passivation. *ChemSusChem* **12**, 983–989 (2019).
33. Eperon, G. E. *et al.* Inorganic caesium lead iodide perovskite solar cells. *J. Mater. Chem. A* **3**, 19688–19695 (2015).
34. SCHERRER & P. Nachr Ges Wiss Goettingen. *Math. Phys.* **2**, 98–100 (1918).

Supplementary materials:

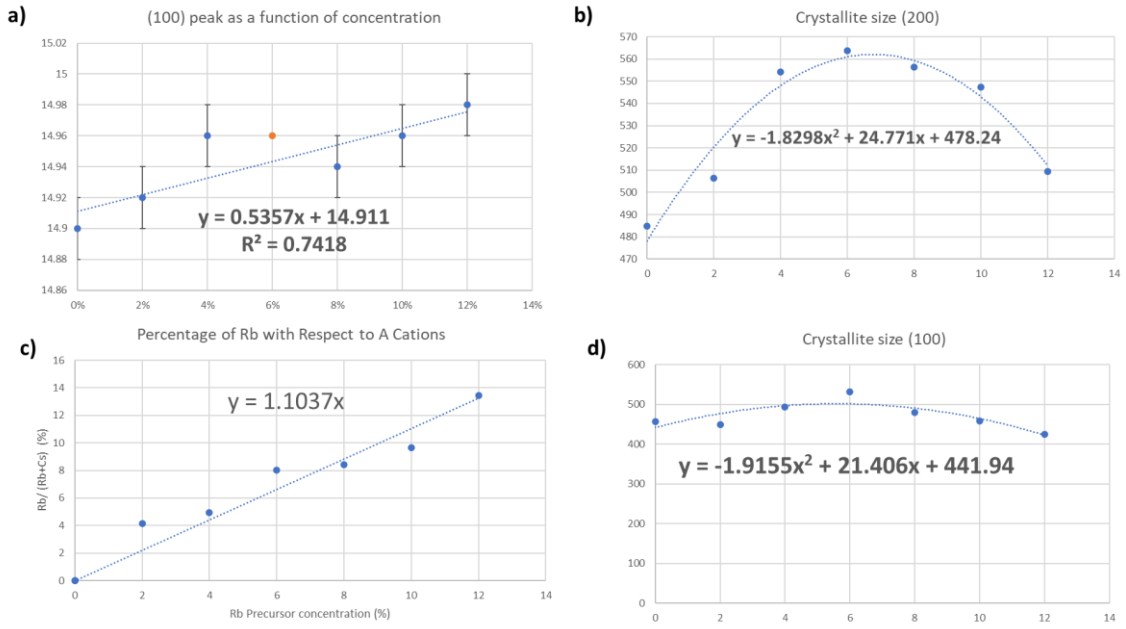

Figure 1: (a) (100) peak as a function of concentration with fitting equation (b) Crystallite size (200) with fitting equation (c) Percentage of Rubidium with respect to Cesium (d) Crystallite size (100) with fitting equation.

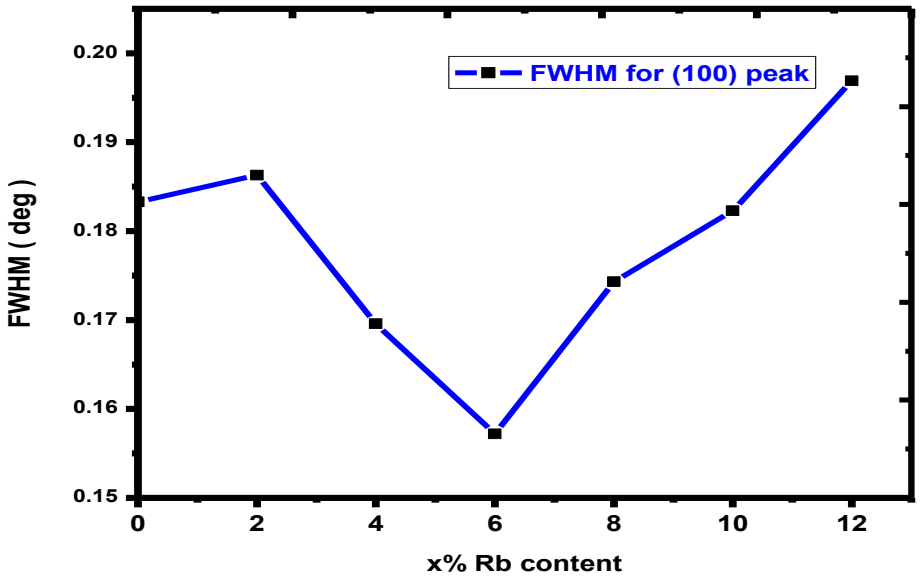

Figure 2: FWHM of the characteristic peak (100) for Cs1-xRbxPbIBr2, where x = 0%, 2%, 4%, 6%, 8%, 10% and 12% thin film.

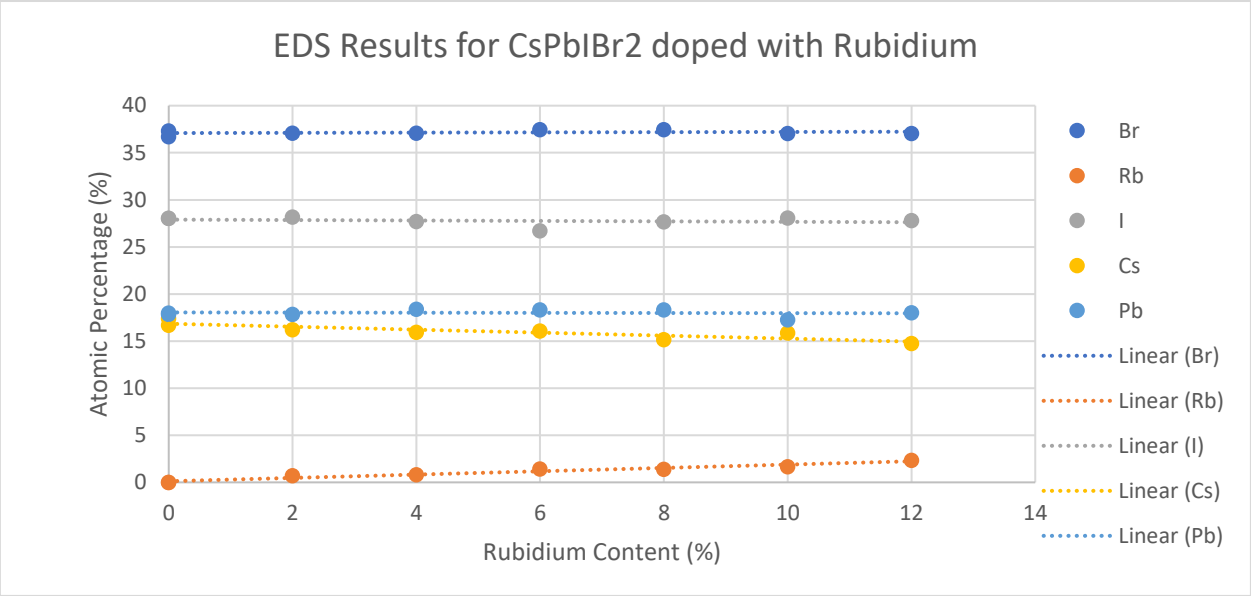

Figure 3: EDS Results for CsPbIBr2 pure and doped with x% Rubidium where x = 0%, 2%, 4%, 6%, 8%, 10% and 12% thin film.

Equation	y = a + b*x	
Plot	PL Primary Pe	Tauc Plot
Weight	No Weighting	
Intercept	2.09779 ± 0.0	2.09786 ± 0.0
Slope	0.00261 ± 5.0	0.00321 ± 5.7
Residual Sum of	1.44429E-4	1.85714E-4
Pearson's r	0.91681	0.92828
R-Square (COD	0.84054	0.8617
Adj. R-Square	0.80864	0.83404

Table 1. Equations and Expressions used for figure 2 and 5 in Manuscript